Large-scale current collectors for regulating heat transfer and enhancing battery safety

Lun Li[1,2,7], Jinlong Yang*[3,7], Rui Tan[4,5,7], Wei Shu[2,3,7], CheeTong John Low[5], Zixin Zhang[2], Yu Zhao[2], Cheng Li[6], Yajun Zhang[6], Xingchuan Li[2], Huazhang Zhang[1], Xin Zhao[1], Zongkui Kou[2], Yong Xiao[2], Francis Verpoort[2], Hewu Wang[6], Liqiang Mai*[2], Daping He*[1,2]

[1]Hubei Engineering Research Center of RF-Microwave Technology and Application, School of Science, Wuhan University of Technology, Wuhan 430070, China
[2]State Key Laboratory of Advanced Technology for Materials Synthesis and Processing, State Key Laboratory of Silicate Materials for Architectures, School of Materials Science and Engineering, Wuhan University of Technology, Wuhan 430070, China
[3]Guangdong Provincial Key Laboratory of New Energy Materials Service Safety, College of Materials Science and Engineering, Shenzhen University, Shenzhen 518060, China
[4]Department of Chemical Engineering, Swansea University, Swansea SA1 8EN, UK
[5]Warwick Electrochemical Engineering Group, WMG, Energy Innovation Centre, University of Warwick, Warwick, CV4 7AL, UK
[6]School of Vehicle and Mobility, Tsinghua University, Beijing 100084, China
[7]These authors contributed equally: Lun Li, Jinlong Yang, Rui Tan, Wei Shu

*Corresponding authors: Jinlong Yang (yangjl18@szu.edu.cn), Liqiang Mai (mlq518@whut.edu.cn), Daping He (hedaping@whut.edu.cn)

Abstract

Thermal runaway, a major battery safety issue, is triggered when the local temperature exceeds a threshold value resulting from slower heat dissipation relative to heat generation inside the cell. However, improving internal heat transfer is challenged by the low thermal conductivity of metal current collectors (CCs) and challenges in manufacturing non-metal CC foils at large scales. Here we report a rapid temperature-responsive non-metallic CC that can substitute benchmark Al and Cu foils to enhance battery safety. The non-metallic CC was fabricated through a continuous thermal pressing process to afford a highly oriented Gr foil on a hundred-meter scale. This Gr foil demonstrates a high thermal conductivity of 1400.8 W m^{-1} K^{-1}, about one order of magnitude higher than those of Al and Cu foils. Importantly, LiNi$_{0.8}$Co$_{0.1}$Mn$_{0.1}$O$_2$‖graphite cells integrated with these temperature-responsive foils show faster heat dissipation, eliminating the local heat concentration and circumventing the fast exothermic aluminothermic and hydrogen-evolution reactions, which are critical factors causing the thermal failure propagation of LIB packs.

Introduction

High-energy lithium-ion batteries (LIBs) with efficient heat transfer capabilities are crucial for ensuring safe operations across various applications, from portable electronics to electric vehicles and grid energy storage transportation[1-4]. Heat in batteries originates from reversible heating due to interfacial charge transfer, overpotential heating from mass transfer and irreversible Joule heating from ohmic polarization[5]. When exposed to harsh treatments, temperature can build up locally due to sluggish heat transfer, leading to a violent thermal runaway upon reaching its threshold value[6-8]. Managing heat generation and improving heat transfer are therefore vital for eliminating thermal runaway of batteries. Although LIB manufacturers have demonstrated well-established battery management systems[9-11] and improved battery configurations[12,13] to monitor the thermal environment of a battery and facilitate heat transfer, significant challenges persist in improving the internal heat transfer and dissipating locally accumulated heat effectively.

In LIBs, current collectors (CCs) are crucial for dissipating heat, maintaining optimal temperatures, and enhancing heat distribution through structural design and material choice[14-17]. Benchmark CCs, primarily composed of the metal families (like Cu and Al), exhibit low thermal conductivities of 200

~ 400 W m^{-1} K^{-1} due to their crystalline structures that scatter electrons and photons, impeding heat flow[18]. In contrast, nonmetallic CCs materials with strong covalent bonds and small atomic mass can result in a higher velocity of phonons, that is, fast particle-core vibrations in a crystal lattice[19], and exhibit enhanced thermal conductivity. As a prototypical nonmetallic material, two-dimensional layered graphene (Gr) exhibits π-π interactions between its layers, leading to a tightly organized stacked structure that facilitates phonon propagation, with a high theoretical conductivity of 600 ~ 5,300 W m^{-1} K^{-1} at room temperature[20-22]. A highly ordered arrangement of graphene sheets and a dense structure can provide an efficient path for heat transfer[23]. Nonetheless, Gr films serving as CCs at large scales present insufficient thermal conduction and mechanical robustness due to the existence of abundant defects and macrovoids, remaining distant from comercialization[24,25]. Given this challenge, it is essential to develop advanced strategies for producing Gr CCs that combine high thermal conductivity, a defect-free structure, crystalline integrity and ease of production.

Considerable effort has been directed towards small-scale fabrication techniques like filtration[26], electro-spray deposition[27], spin-coating[28] and dip-coating[29], all of which have successfully produced free-standing Gr films used in coin-type batteries. However, scaled-up production of uniform Gr films for the continuous manufacturing of commercial LIBs, particularly high-energy batteries that typically require a CC area of 100 ~ 1,000 m^2, remains challenging[16,17]. Furthermore, the limited flexibility, inadequate tensile strength and brittleness of current Gr films pose challenges for pouch-type cell manufacturing, particularly incorporation into the winding process of electrodes and the welding process with tabs. As such, there is a need for preparing large-scale, dense and defect-free Gr CCs for enhancing the safety of LIBs.

In this study, we report the large-scale production of thermally conductive nonmetal CCs as effective substitutes for benchmark metallic foils to effectively mitigate deleterious thermal issues and enhance battery safety. A continuous thermal compression process was developed to produce dense, defect-free and flexible Gr foil at a hundred-meter scale, matching the requirements of large-sized energy-storage devices, such as lithium-ion pouch cells, redox flow batteries, electrolysers and fuel cells. Importantly, this Gr foil with a high thermal conductivity of up to ~1401 W m^{-1} K^{-1} can regulate heat transfer and enhance thermal tolerance, eliminating exothermic aluminothermic and hydrogen-evolution reactions in stress-tested batteries. The rapid thermally responsive Gr foil can maintain a more uniform heat distribution during fast charging/discharging and reduce the temperature of a short-circuited cell to ~150 °C, preventing combustion and explosion. Most importantly, the working principles of Gr CCs for fast heat dissipation and the prevention of thermal issues are comprehensively studied. These lightweight and electrically conductive Gr CCs also enable LIBs to operate with increased output energy and power. The design of the nonmetal Gr foil offers a promising strategy for simultaneously enhancing thermal safety and energy density in large-scale energy-storage solutions.

Results

Large-scale manufacturing of the Gr foil

The fabrication of the Gr foil was achieved via a continuous large-scale manufacturing protocol using dispersed graphene oxide (GO) with the addition of 3.0 wt.% phenethylamine (PEA). As illustrated in **Fig. 1a** and Extended Data **Fig. 1**, GO/PEA-assembled hybrid films were first prepared via a continuous process of coating, rolling and drying on a polymeric substrate. As a "molecular welder" with a benzene ring, PEA chains were intercalated between GO sheets. Notably, GO hybrid films were achieved on meter and kilometer scales, depending on the dimensions of the manufacturing apparatus (Supplementary **Fig. 1b**). Thereafter, the precursor film underwent a carbonization process to improve the film quality by removing impurity elements at 1500 °C. The carbonized PEA formed sp^2 graphitized carbon layers, which exhibit strong π-π attractions with graphene sheets, thereby facilitating the formation of highly aligned and dense films (Supplementary **Fig. 1a**). The proliferation of six-membered rings can increase the domain size of the graphene film and eliminate the generation of defects during thermal decomposition, which can produce a highly oriented and strong Gr film with preferred 2D graphitic crystallinity at 2850 °C [30] (Supplementary **Fig. 2-5**,

Extended Data **Fig. 2** and Supplementary **Note 1**). Continuous rolling compression was performed to tune the thickness of Gr film according to the application demands. The entire film exhibits a dense morphology without any observable cracks and voids (**Fig. 1b**, **c**), indicative of sufficient structural integrity throughout the heating process. SEM images (**Fig. 1c**) show that abundant microfolds are distributed on the surface of Gr foil after carbonization and graphitization. After rolling, these intrinsic microfolds remain, enhancing the roughness of Gr surface and contributing to the tight interfacial contact between electrode materials and Gr CCs. This tight contact facilitates the transfer of electrons and locally generated heat. The final thickness of Gr CCs can be precisely controlled at 17 ± 1 µm after continuously rolling (**Fig. 1c**). The adjustable lengths reaching up to 200 m can be easily achieved (**Fig. 1d** and Supplementary **Fig. 1c**), of which an effective area of 200×0.6 m^2 surpasses those of the previously reported graphene-based films (**Fig. 1e**, Supplementary **Table 1**).

The uniformity of properties in scaled-up CCs is crucial as it dictates the even distribution of current and heat, the utilization of active materials as well as the discharge depth, which subsequently affects heat transfer, aging and localized failure[31]. Previous studies have concentrated on the properties of CCs on a relatively small scale, without focusing on how the resulting properties might change or be affected when the products are scaled-up[26,32]. In contrast, our meter-scale Gr foil exhibits a highly uniform thickness (17 ± 1 µm), electrical conductivity ($1.3 \pm 0.02 \times 10^6$ S m^{-1}) and thermal conductivity (1400.8 ± 9.6) W m^{-1} K^{-1} (Supplementary **Fig. 5**, **Table 2**), suggesting the potentially safe and efficient functioning of batteries when produced at a commercially-relevant level.

Characterizations of the thermally responsive Gr foil

The structural integrity and defect-free morphology are studied further via XRD, Raman spectra and high-resolution TEM. The sharp (002) diffraction peak of the Gr foil is located at 26.47°, corresponding to graphitized carbon with an interlayer distance of d = 3.36 Å (**Fig. 2a**). The Raman spectra show the I_D/I_G ratio is 1.04 for the GO film; this value dramatically dropped to near zero for Gr foil (**Fig. 2b**) due to defect self-repairing (internal heteroatom defects in the GO, vacancies or interstitial atoms in the C film, and poor crystallographic orientation in the Gr film) and generation of ordered structure during the high-temperature graphitization process. Asymmetric peak of the 2D band is deconvoluted into 3 Lorentzian peaks which indicates the amount of AB-stacked and turbostratic regions. (Supplementary **Fig. 6**). Consistent with Raman spectra, HR-TEM top-view images confirm further the defect-free structure of the Gr foil with a regular long-range planar hexagonal lattice (**Fig. 2c**, Supplementary **Fig. 7**). The white and red hexagons correspond to the odd and even graphene layers, aligning with the AB stacked graphene structure. This suggests that this Gr configuration is the energy minimum state[20,33]. HR-TEM images show the highly aligned lattice fringe with interplanar distances of 0.247 nm and 0.336 nm, corresponding to the (110) and (002) planes of graphitic carbon, respectively (**Fig. 2c, d**). This highly oriented and defect-free structure enhances the film mechanical properties, as evidenced by the high tensile strength of 81.6 MPa (**Fig. 2e**, Supplementary **Fig. 8**).

Heat transfer and electron conduction are intertwined factors that influence the performance of CCs. The Gr film exhibits a high thermal conductivity of 1400.8 ± 9.6 W m^{-1} K^{-1}, about one order of magnitude higher than benchmark Cu and Al CCs, or 187.8 ± 0.3 and 166.1 ± 0.5 W m^{-1} K^{-1}, respectively (**Fig. 2f**, Supplementary **Table 3**). This high thermal conductivity allows more rapid thermal transfer, as visually evidenced by thermal images (Supplementary **Fig. 9a**). Gr films coated with redox species still maintain a high heat transfer rate, resulting in a more uniform heat distribution of the Gr-based electrode (Supplementary **Fig. 9b**). We further investigated the cooling behaviors of Gr-film-incorporated cells after being heated to 60 °C. Cells with Gr films clearly displayed a more uniform heat distribution and a lower overall temperature, compared to the cells with Al and Cu CCs (Supplementary **Fig. 10**). With continuous pathways for electrons, the Gr film also presents high electrical conductivity (**Fig. 2g**) and low mass density (Supplementary **Table 3**), indicating its potential for further promoting the energy output of devices. The electrical conductivity of $(1.3 \pm 0.02) \times 10^6$ S m^{-1} in our work surpasses previously reported carbon-based CCs (**Fig. 2h** and

Supplementary **Table 4**).

Besides fast heat and electron transfer, the densified Gr film exhibits enhanced flexibility. The flexibility and durability are evaluated upon repeated bending, curling, and folding into an airplane (**Fig. 2i-k**); especially upon folding 180°, the dense microstructure is still maintained without any breakage (**Fig. 2l**), illustrating sufficient flexibility. As displayed in **Fig. 2m**, the Gr foil can retain its high conductivity under bending over 100,000 times. The flexibility of the Gr film suggests its potential applicability within large-scale production lines, especially in the continuous and large-scale coating of redox-species slurries and in the automated rolling process of electrodes (Supplementary Video 1-2). More importantly, the densified Gr film enabled robust soldering of cell tabs via an ultrasonic-assisted soldering technique[36,37] and further enabled a tight connection of cell accessories (Supplementary **Fig. 11**, **12**). Given the capabilities in rapid heat and electron transfer combined with robust mechanical properties, we believe our Gr films are promising non-metallic CCs (or foils for simplicity).

Large-scale manufacturing of LIB pouch cells

To demonstrate the advantages of Gr foils in large-scale LIB manufacturing, practical pouch cells were assembled using $LiNi_{0.8}Co_{0.1}Mn_{0.1}O_2$ (NCM811) cathodes and graphite anodes with Gr foil as CCs on both sides, denoted as Gr‖Gr cells (**Fig. 3a**). The pouch cells with Al and Cu CCs, namely Al‖Cu cells, were prepared as control samples (Supplementary **Tables 5** and **6**). As demonstrated in **Fig. 3b**, our engineered Gr foil seamlessly integrates with the continuous assembly for lithium-ion pouch cells with varied capacities (2-10 Ah), which includes single- and double-sided coating procedures, an automated electrode winding process, welding the Gr CCs to metal tabs, and the successfully assembled Gr‖Gr pouch cells. In addition, 5 Ah and 10 Ah pouch cells can also be prepared using stacked electrodes (Supplementary **Fig. 13-14**, Extended Data **Fig. 3a-c**), further demonstrating the practical potential of our Gr CC for manufacturing high-capacity batteries.

Furthermore, the electrochemical performance of pouch cells with both (non)metal CCs were evaluated, in which both cells exhibited comparable working voltage plateaus, confirming the applicability of Gr foils in practical cells (Supplementary **Fig. 15**). The Gr‖Gr cell maintained a high discharge capacity of 186.0 mAh g^{-1} with a retention of 89.2% over 1000 cycles at 1 C (Supplementary **Fig. 16**). Since the Gr foil possesses a lower weight density, our Gr‖Gr cell delivered an initial energy density of 271.9 Wh kg^{-1} and an energy density of 241.6 Wh kg^{-1} after 1000 cycles, surpassing the energy density of the Al‖Cu pouch cell (**Fig. 3c**). In addition, the Gr‖Gr pouch cell shows higher rate capability (77.5%) with a higher discharge capacity of 154.5 ± 4.9 mAh g^{-1} at 4 C than those of the Al‖Cu cell (60.2%, 120.7 ± 1.9 mAh g^{-1}) (**Fig. 3d**), attributing to a reduced interface transfer resistance as further evidenced by contact angle, EIS results and high electrochemical stability during cycling (Supplementary **Fig. 17-20**, Extended Data **Fig. 4**, Supplementary **Table 7** and **Note 2**).

Energy storage and conversion invariably lead to heat generation and temperature fluctuations. Temperature variance of pouch cells during fast cycling at a high current was visually recorded using *operando* infrared thermography (**Fig. 3e-3f**). In both cells, the internal temperatures rise over constant-current charging and gradually decrease over constant-voltage charging, while their temperatures increase depending on the depth of discharge, which suggests the risky periods of stages IV and IX for inducing thermal issues. Compared to the Al‖Cu cells, the Gr‖Gr cell with fast temperature-responsive CCs can enable fast heat transfer from inside to outside, resulting in a lower maximum temperature (**Fig. 3g**) and a more uniform heat distribution (**Fig. 3f** and Supplementary **Fig. 21-22**). As shown in **Fig. 3h**, the heat-concentrated region at L'=L/L$_0$ ≈ 0.4 for the Al‖Cu cell can easily become the initial trigger point of thermal runaway. Such a temperature gradient can induce the changes of current density and various failures in electrodes, which can accelerate aging and thermal issues[39]. The temperature of the Gr‖Gr pouch cell stabilizes at a relatively same value and gets slightly lower at the anode tab. The superior heat transfer and thermal management abilities of Gr CCs are further proved by simulation results where the heat produced by the soldering point and

the inner reaction are taken into consideration (Supplementary **Fig. 23**). Even with 10 Ah pouch cells, the peak temperature during fast discharging at 2 C (54.8 °C) remains significantly lower than that of a 2.3 Ah 18650-cylindrical cell at 3 C where the maximum temperature exceeds 70 °C[39] (Extended Data **Fig. 3d-e**). Furthermore, a portable charger with an output voltage of 5 V and a current of 3 A has been created from a 2 Ah battery (Supplementary **Fig. 24**), effectively charging a mobile phone (Supplementary Video 3). Heat within the battery is uniformly distributed throughout the entire charging process without noticeable temperature fluctuation.

Regulation of heat transfer in stress-tested batteries

To confirm the improvement of safety performance using Gr CCs, we investigated the thermal characteristics and emitted gases of four assembled pouch cells with Al‖Cu, Al‖Gr, Gr‖Cu, and Gr‖Gr CCs via the thermal runaway test and gas analysis system (**Fig. 4a**). The charged pouch cells were placed in the chamber (Supplementary **Fig. 25**, **26**) where temperature and pressure were monitored under stress-tested conditions. The total emissions of exhaust gases mainly consisting of H_2, CO, CO_2, C_2H_4, CH_4 and C_2H_6 for Al‖Cu, Al‖Gr, Gr‖Cu and Gr‖Gr were 360, 350, 270 and 240 mmol, respectively (Supplementary **Fig. 27, 28**). CO_2 is a decomposition product of electrolyte thus indicating the intensity of the redox reaction during the thermal runaways process[40,41]. Notably, the contents of flammable H_2, CO and C_2H_4 are greatly reduced in the pouch cell with Gr CCs (**Fig. 4b**), confirming that Gr CCs can effectively suppress the risk of battery ignition and explosion under harsh stress tests, which is further evidenced by the unfold electrodes from stress-tested batteries (Supplementary **Fig. 29**). Compared to Al‖Cu pouch cells, the Gr‖Gr cells with fast temperature-responsive ability showed a much lower peak temperature of 130 °C and a delayed onset of 120 s of the self-sustaining exothermic reactions during thermal runaway (**Fig. 4c**). **Fig. 4d** compares the maximum temperature ($T_{max.}$) of stress-tested batteries based on NCM811 cathodes, among which nonmetal Gr CCs exhibited the lowest $T_{max.}$ and ensured stress-tested batteries in a safer region (Supplementary **Table 8**).

The temperature-responsiveness of the CCs was investigated by thermogravimetry and differential scanning calorimetry (TG-DSC), which clearly explore the structural stability of metallic CCs at high temperatures (Supplementary **Fig. 30**). The Cu CC presents fast heat release attributed to the oxidation of Cu (Supplementary **Fig. 31**) while Al melted at 659 °C with the generation of numerous cracks and pinholes on the Al foil, which inevitably lost its structural integrity and mechanical strength. The completion of structural destruction only lasted for 30 s in fire where Al foil plays (Supplementary **Fig. 32-33**). The Al foil therefore plays a critical role in inducing and deteriorating the process of thermal runaways as well as destroying the structure of electrode materials (Supplementary **Fig. 34-35**). As described in **Fig. 4e**, Al and Cu CCs with relatively poor thermal conductivities cannot transfer the locally generated heat timely followed by the separator melting, leading to internal short circuit of the battery. Then, the exothermic reaction inside the battery is triggered and temperature is increased companied by the organic electrolyte decomposition to generate flammable gas including H_2, CO and C_2H_4. As the temperature rises to the ignition temperatures of these gases (C_2H_4: 490 °C, H_2: 572 °C, CO: 609 °C)[42], the representative chemical reactions occur in sequence, as shown in Eq. 1-3.

$$C_2H_4 + 3O_2 \rightarrow 2CO_2 + 2H_2O \qquad\qquad (1)$$
$$2H_2 + O_2 \rightarrow 2H_2O \qquad\qquad (2)$$
$$2CO + O_2 \rightarrow 2CO_2 \qquad\qquad (3)$$

Once the temperature reaches nearly 660 °C, Al is prone to aluminothermic reactions with its nearby NCM811 oxide active material (Eq. 4)[43-46], rapidly releasing large amounts of heat, resulting in a strong jet flame and sparks, which determines whether thermal runaway can occur.

$$4Al + 3MO_2 \ (M=Ni/Co/Mn) \rightarrow 3M + 2Al_2O_3 \qquad\qquad (4)$$
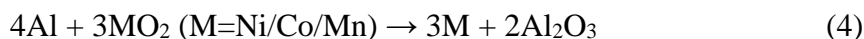
In contrast, Gr CCs retained structural integrity (Supplementary **Fig. 29**, **36-37**) and maintained high flexibility and electrical conductivity even at 800 °C (Supplementary **Fig. 38-39**). The dense structure

remained over the thermal runaway process, efficiently obstructing the O_2 entry and preventing the ignition[47-50] (Supplementary **Fig. 40-41**). More importantly, Gr foils with thermal stability and high thermal conductivity can easily transfer the heat outward from hotspots and effectively circumvent exothermic reactions when encountering abnormal thermal triggers, largely reducing the generated gas and resulting in lower and more even temperature distribution (**Fig. 4f**).

The nail-penetration test, a prototypical safety test in extreme LIB analyses, serves as a measure for evaluating the thermal resilience of cells using Gr CCs. Using a sharp nail, the charged pouch cells were penetrated at its center at a rate of 0.75 mm s^{-1}. The pouch cell using Al and Cu CCs exhibited rapid swelling within 4 s, accompanied by heavy smoke and a persistent flame emanating from the negative terminal and penetration site (**Fig. 4g** and Supplementary Video 4). The predominant components of the smoke are organic vapors from liquid electrolytes, evolving into flammable gases, resulting in an intense combustion lasting for 42 s until all combustibles are depleted. In contrast, the penetrated pouch cell with Gr CCs exhibited minor swelling and produced slight smoking without noticeable fire (**Fig. 4h** and Supplementary Video 5), validating considerably enhanced fireproofing. Nail penetration towards 5-Ah batteries further confirms that Gr foils can prevent thermal issues of high-capacity batteries (Extended Data **Fig. 3f** and Supplementary Video 6, Supplementary **Fig. 42**). Interestingly, compared to the metallic CCs, nonmetal CCs with a remarkable ability for heat transfer can quickly dissipate local heat and maintain their structures during thermal runways (**Fig. 4i-4j**, Supplementary **Fig. 43**). Reproducible nail penetration tests using same or different needle testers on more than ten cells with Gr foil as CCs to confirm its reproducible performance (Supplementary **Fig. 44**).

Transient finite element simulations were further employed to investigate the heat transfer inside the practical pouch cells with Gr film and benchmark Cu and Al CCs. Short circuiting is a critical initiating factor that leads to thermal runaway in a short time, which was designated as the specific scenario in our modeling. As a result, the heat distribution of a short-circuit cell with Al and Cu CCs accumulates in 0.2 s where the local temperature rapidly rises above 250 ℃ and then quickly expands and induces battery thermal runaway within 1 s (Supplementary **Fig. 45-46**). In comparison, the maximum temperature of the cell with Gr films is less than 150 ℃, and the overall temperature quickly drops to room temperature, clearly showing that the Gr foil features fast temperature-responsive performance and efficiently regulates heat transfer within stress-tested cells.

Discussion

The strategy of regulating internal heat transfer and mitigating thermal issues for batteries was realized by tuning the thermal properties of the CCs. We introduced a nonmetal CC, that is, Gr foil, engineered for rapid heat dissipation using a continuous and large-scale thermal compression method. This CC possesses important properties, for example, a dense and defect-free structure, remarkable flexibility like the metal foil, ease-of-manufacturing performance suggesting at potential large-scale fabrication, as well as a high thermal conductivity. Benefiting from these attributes, particularly the thermal performance, Gr foils can effectively regulate the heat transfer both in the normal and stress-tested batteries, largely reducing the risk potential of thermal issues. For the operation of LIBs, lightweight Gr foils can further enhance the energy and power densities, resulting in the improved energy density of 271.9 Wh kg^{-1} over 1,000 cycles for practical NCM811‖graphite pouch cells. The development of 10-µm-thick Gr foils (Supplementary **Table 9**, Extended Data **Fig. 5** and Supplementary **Note 3**, Supplementary **Fig. 47**) with a lower specific mass of 2 mg cm^{-2} is anticipated to further enhance the gravimetric energy density of the battery to 289.9 Wh kg^{-1} and increase the volumetric energy density to levels comparable to commercial batteries used in mobile phones, drones and electric vehicles. This work also offers a comprehensive study on the mechanisms behind heat transfer regulation and battery failure, shedding light on the design of future thermo-responsive, safe and conductive CCs. Importantly, these advanced CCs are versatile and suitable for diverse electrochemical applications like electrolysers, fuel cells and redox flow batteries, paving the way for potentially efficient and intrinsically safe large-scale energy solutions.

Methods

Gr foil fabrication. Large flake size GO (purchased from Wuxi Chengyi Education Technology Co., Ltd.) was selected as the building precursor of the Gr foil. First, the GO solution with a concentration of 30 mg mL^{-1} was homogeneously mixed with 3 wt.% PEA to form a uniform hydrogel. Then, the GO-based hydrogel was transferred on a polyethylene terephthalate (PET) film by the pre-metered roll coating method. Subsequently, the GO film was mildly dried at 70 °C using the large drying oven. Thereafter, the large size GO film was peeled from the PET film and regularly cut into the desired width. The resulting GO film was annealed in Ar atmosphere for carbonization (1500 °C) and graphitization (2850 °C) to obtain the graphene-assembled film. Finally, the obtained GAF was continuously rolled under a pressure of 200 MPa to obtain dense Gr foils with high electrical conductivity, high thermal conductivity, and improved mechanical strength.

Microstructural characterization. X-ray diffractometer (XRD) characterizations were performed by a Bruker D8 Discover X-ray diffractometer with Cu Kα radiation (λ = 1.054056 Å). Raman spectra was obtained with an excitation laser of 532 nm by Horiba LabRAM HR Evolution. X-ray photoelectron spectroscopy (XPS) was determined by the VG MultiLab 2000 instrument. Fourier transform-infrared (FTIR) transmittance spectra were measured using a Nicolet 60-SXB IR spectrometer. Thermogravimetric analysis (TGA) was carried out on a NETZSCH STA 449F5 instrument. The surface and cross-sectional morphology were observed by SEM with a JEOL-7100F scanning electron microscope and a 3D microscope with ultra-depth field (KEYENCE VH-Z500R). The contact angles were acquired by an OCA 35 data physics instrument. The stress-strain curves were obtained by a universal testing machine (MTS E44.104, 0.3 mm/min). Infrared thermal images were collected using a ST9450 thermal imaging camera. The thermal conductivity was tested by the laser flash method using Netzsch LFA 467 NanoFlash system.

Electrode preparation. The cathode was composed of 94.0 wt.% LiNi$_{0.8}$Co$_{0.1}$Mn$_{0.1}$O$_2$ (T85RS-N-20010-S2，200 mAh g^{-1}), 4.0 wt.% Super P conductive carbon black and 2.0 wt.% polyvinylidene fluoride binders. To obtain the Al/NCM811 and Gr/NCM811 electrodes, the slurry was coated onto both sides of Al foil and Gr CC, respectively, by using a continuous coating machine with velocity of 1.3 m min^{-1} in a dry room. After drying and subsection calendaring (500 psi), the press density of cathode was controlled at (34.4 ± 3.0%) mg cm^{-2}. The anode was composed of 95.2 wt.% graphite (340 mAh g^{-1}), 1.0 wt.% Super P conductive carbon black, 1.5 wt.% sodium carboxymethyl cellulose (CMC) and 2.3% Styrene-butadiene rubber (SBR). The slurry was subsequently coated onto both sides of Cu foil and Gr CCs, respectively, by using a continuous coating machine with velocity of 2.0 m/min. After drying and calendaring (500 psi), the press density of anode was controlled at (21.0 ± 3%) mg cm^{-2}.

Full cell assembly and Testing. Pouch cells were assembled with a semi-automated cell-manufacturing line which comprises the cathode, anode and separator; grid-trim; curling, pulse resistance welding for connection with Al (cathode) and Ni coated Cu (anode) external tabs; packaging and vacuum sealing with electrolyte injection. For one pouch cell, the coating area of cathode and anode layer were designed as 85×445 mm and 86.5×565 mm. After curling, an 8-layer cathode and 9-layer anode were sandwiched by the separator to form the core. For all the full batteries, the N/P ratio is 1.05. The specific energy density is calculated based on the mass of cathode, anode, CCs, conductive additive, binder and separators.

Galvanostatic discharge/charge tests were conducted by a multichannel testing system (LAND CT2001A). The EIS measurements were carried out using an Auto lab PGSTAT 302N electrochemical workstations. Gr‖Gr pouch cells for cycling were charged using constant current (1 C) - constant voltage (4.25 V) until the current decreased to 0.05 C and discharged using constant current (1 C) to 3 V. Gr‖Gr pouch cells for rate performance were charged using constant current (0.2 C) - constant voltage (4.25 V) until the current decreases to 0.05 C and discharged using various constant current (0.2-3 C) to 3 V. For performance at 4 C, pouch cells were charged using constant

current (4 C) - constant voltage (4.25 V) until the current decreased to 0.4 C and discharged at 4 C to 2.8 V. During testing, the pouch cell was positioned between two flat glass plates, which were then secured using a metal clamp. An operational pressure of ~2.94 MPa was applied to the glass plates through these metal clamps.

Electrical conductivity measurements. The electrical conductivities of various films are measured by a Four-Point Probes Resistivity Measurement System (Probes Technology, RTS-9). First, samples with size of 10 mm×10 mm was selected to test the volume resistivity. Then the conductivity is calculated by the Eq. 5:

$$\sigma = 1/(\rho_0\,W) \tag{5}$$

Where W is the thickness of the sample and ρ_0 is the tested volume resistivity.

Thermal conductivity measurements. Thermal conductivities were tested by NETZSCH LFA 467 NanoFlash instrument by the laser flash method according to the standard test method ASTM E1461. The test sample was cut into a disc with diameter of 2.46 cm. The thermal diffusivity is obtained from the temperature-time curve using the following Eq .6

$$\alpha = 0.1388\,d^2(t_{50})^{-1} \tag{6}$$

In Eq. 6, α is the tested thermal diffusivity, d is the thickness of the sample, and t_{50} is half of the diffusion time (surface temperature of the test sample rises to the maximum temperature after receiving irradiation of optical pulse).

The thermal conductivity (K) is calculated according to the following Eq. 7:

$$K = \rho C_P \alpha \tag{7}$$

where, ρ is the density of the tested sample, which is obtained based on ρ=m/V, where m and V are the mass and volume of the test sample, respectively. Specifically, ρ_{rGO}=0.27 g cm^{-3}, ρ_{GAF}=0.29 g cm^{-3}, ρ_{Gr}=2.15 g cm^{-3}, and C_p (0.8 J g^{-1} K^{-1}) is the specific heat capacity of graphene.

Needling testing: In the nail penetration testing, a needle machine (model: SRCN-1000N) with a steel nail with a diameter of 5 mm and a speed of 0.75 mm/s was used to penetrate the whole cells to observe whether the battery burns or explodes.

Gas collection and detection in thermal runaway. The thermal runaway is triggered by external heating in a sealed chamber with a volume of 230 L. The chamber can endure an inner pressure of 3 MPa and the heating power of the electric heater is 150 ~ 200 kW. Before heating the cells, the chamber was repeatedly evacuated and flushed with N_2 to ensure the air content less than 1%. The batteries were fixed horizontally to the heater using the same preload. The vent gas emissions were sampled using a gas bag when the temperature and pressure in the rector were stable for a while. Finally, the gas components were analyzed by the GC system (Trace1300).

Phase field simulation. The finite element method is used to solve energy balances for the temperature distribution of the battery during operation. The heat conduction in the battery, as well as the heat convection and radiation at the surfaces are taken into consideration for a stationary simulation. The heat produced by polarization at two connection between cathode/anode and tabs, as well as the inner electrochemical reaction are taken into consideration.

Data availability
All data are available in the main text or Supplementary Information. Source data are provided with this paper.

Author contributions

L.L., J.Y., R. T., L.M. and D.H. conceived and directed the project. L.L. and W.S. carried out the syntheses, characterizations and battery testing. L.L. wrote the original draft. R.T., X.L. and Z.Z. assisted in visualizing the manufacturing process and working principles. C.L., Y.Z. and H.W. helped perform the TR tests and analyse the data. Y.Z. and Y. X. guided the welding of CCs with metal tabs. R.T., C.T.J.L. and H.Z. contributed to theory and model development. L.L., J.Y., R.T, X.Z., Z.K., F.V., L.M. and D.H. revised the manuscript and suggested for details in tests. All authors participated in the discussion of the results, commented on the implications, and fully approved the content of the manuscript.

Competing Interests

The authors declare no competing interests.

Figure Captions.

Fig. 1 | Fabrication of the large-area Gr foil. a, Schematics showing a continuous thermal pressing process for fabricating Gr foil. **b**, Photos and **c**, surface SEM images of GO film, carbon (C) film, Gr film, and Gr foil, inset: the corresponding cross-sectional images. **d**, Image of large-scale Gr foil (200 × 0.6 m^2) taken using an unmanned aerial vehicle on the ground of a standard track field. **e**, Comparison of the Gr foil areas produced in this work and to those reported in literatures.

Fig. 2 | Foil physical characterization. a, XRD analysis of GO, C film, Gr film, and Gr foil patterns. **b**, Raman spectra of GO, C film, Gr film, and Gr foil. **c**, High-resolution TEM image of the Gr nanosheets from top-view and **d**, cross-sectional view. **e**, Stress-strain curves of Gr foil. **f**, Thermal conductivities of the Gr foil and the benchmark Al and Cu foils (n=10). **g**, Electrical conductivities of GO film, C film, Gr film and Gr foil (n=10). **h**, Comparison of electrical conductivities of Gr CCs with previously reported values in the literature. Flexibility demonstrations under various deformation conditions: **i**, bending, **j**, curling, **k**, folding into an airplane; **l**, cross-sectional SEM images of Gr foil folded at 180°. **m**, Resistance alternation of Gr with 100,000 repeated bending tests. Data are presented as mean ± SD. The error bars represent standard deviation from ten independent measurements.

Fig. 3 | Electrochemical and thermal performance. a, Schematic diagram of a pouch cell integrated with Gr CCs. **b**, Assembly of Gr||Gr pouch cells. **c**, Specific energy of pouch cells using Gr||Gr and Al||Cu foils over 1000 cycles at 1 C. **d**, Specific capacity and capacity retention at different current rates from 0.2 to 4 C (n=3). **e**, Fast charging and discharging profiles of a pouch cell with Gr||Gr foils at 4 C. **f**, Temperature distribution at different stages. **g,** Maximum temperatures at stage IV (red bar) and stage IX (blue bar) with the maximum temperature difference (red symbols) at stage IX. **h**, Simulated and experimental thermal behavior for the pouch cells with Gr||Gr and Al||Cu foils at stage IV. Data are presented as mean ± SD. The error bars represent standard deviation from three independent measurements.

Fig. 4 | Safety performance and mechanism analysis of pouch cells during thermal runaway. a, Schematic diagram of the thermal runaway experimental settings with gas collection and detection. The inset shows the photo of the sealed chamber where thermal runaway occurs. **b**, Specific molar content of each gas composition after thermal runaway for Al||Cu and Gr||Gr pouch cells (n=3). **c**, Temperature profiles of fully charged Al||Cu and Gr||Gr pouch cells during thermal runaway. **d**, Comparison of the battery safety between this work and other publications based on NCM811 cathode under TR. **e**, Incendiary explosion reaction mechanism of Al||Cu cells during thermal runaway. **f**, Safety improvement mechanism of Gr||Gr cells. **g**, **h**, Nail penetration test on the assembled (g) Al||Cu, (h) Gr||Gr pouch cells. **i**, **j**, Unfold electrodes inside (i) Al||Cu and (j) Gr||Gr

pouch cells after nail penetration. Data are presented as mean ± SD. The error bars represent standard deviation from three independent measurements.

References

1. Liu, H. et al. A disordered rock salt anode for fast-charging lithium-ion batteries. *Nature* **585**, 63-67 (2020).

2. Turcheniuk, K., Bondarev, D., Singhal, V. & Yushin, G. Ten years left to redesign lithium-ion batteries. *Nature* **559**, 467-470 (2018).

3. Needell, Z. A., McNerney, J., Chang, M. T. & Trancik, J. E. Potential for widespread electrification of personal vehicle travel in the United States. *Nat. Energy* **1**, 16112 (2016).

4. Goodenough, J. B. & Kim, Y. Challenges for rechargeable Li batteries. *Chem. Mater.* **22**, 587-603 (2010).

5. Song, L., Zheng, Y., Xiao, Z., Wang, C. & Long, T. Review on thermal runaway of lithium-ion batteries for electric vehicles. *J. Electron. Mater.* **51**, 30-46 (2022).

6. Feng, X., Ren, D., He, X. & Ouyang, M. Mitigating thermal runaway of lithium-ion batteries. *Joule* **4**, 743-770 (2020).

7. Wang, Z., Yang, H., Li, Y., Wang, G. & Wang, J. Thermal runaway and fire behaviors of large-scale lithium ion batteries with different heating methods. *J. Hazard. Mater.* **379**, 120730 (2019).

8. Li, Y. et al. Thermal runaway triggered by plated lithium on the anode after fast charging. *ACS Appl. Mater. Interfaces* **11**, 46839-46850 (2019).

9. Longchamps, R. S., Yang, X. G. & Wang, C. Y. Fundamental insights into battery thermal management and safety. *ACS Energy Lett.* **7**, 1103-1111 (2022).

10. Yang, X.-G., Liu, T. & Wang, C.-Y. Thermally modulated lithium iron phosphate batteries for mass-market electric vehicles. *Nat. Energy* **6**, 176-185 (2021).

11. Wang, C. Y. et al. Lithium-ion battery structure that self-heats at low temperatures. *Nature* **529**, 515-518 (2016).

12. Wang, C., He, L., Sun, H., Lu, P. & Zhu, Y. Battery pack, vehicle and energy storage device. China Patent CN110165118B (2019).

13. Huang, W., Feng, X., Han, X., Zhang, W. & Jiang, F. Questions and answers relating to lithium-ion battery safety issues. *Cell Reports Phys. Sci.* **2**, 100285 (2021).

14. Janna, W. S. *Engineering Heat Transfer*. CRC Press, (2018).

15. Ye, Y. et al. Ultralight and fire-extinguishing current collectors for high-energy and high-safety lithium-ion batteries. *Nat. Energy* **5**, 786-793 (2020).

16. Liu, Z. et al. Stretchable separator/current collector composite for superior battery safety. *Energy Environ. Sci.* **15**, 5313-5323 (2022).

17. Choudhury, R., Wild, J. & Yang, Y. Engineering current collectors for batteries with high specific energy. *Joule* **5**, 1301-1305 (2021).

18. Dai, W. et al. Metal-level thermally conductive yet soft graphene thermal interface materials. *ACS Nano* **13**, 11561-11571 (2019).

19. Balandin, A. A. Thermal properties of graphene and nanostructured carbon materials. *Nat. Mater.* **10**, 569-581 (2011).

20. Balandin, A. A. et al. Superior thermal conductivity of single-Layer graphene. *Nano Lett.* **8**, 902-907 (2008).

21. Faugeras, C. et al. Thermal conductivity of graphene in corbino membrane geometry. *ACS Nano* **4**, 1889-1892 (2010).

22. Han Z., Ruan, X. Thermal conductivity of monolayer graphene: Convergent and lower than diamond. *Phys. Rev. B* **108**, L121412 (2023)

23. Xin, G. et al. Highly thermally conductive and mechanically strong graphene fibers. *Science* **349**, 1083-1087 (2015).

24. Seol, J. H. et al. Two-dimensional phonon transport in supported graphene. *Science,* **328**, 213-216 (2010).

25. Peng, L. et al. Ultrahigh thermal conductive yet superflexible graphene films. *Adv. Mater.* **29**, 1700589 (2017).

26. Chen, Y. et al. Reduced graphene oxide films with ultrahigh conductivity as Li-ion battery current collectors. *Nano Lett.* **16**, 3616-3623 (2016).

27. Beidaghi, M., Wang, Z., Gu, L. & Wang, C. Electrostatic spray deposition of graphene nanoplatelets for high-power thin-film supercapacitor electrodes. *J. Solid State Electrochem.* **16**, 3341-3348 (2012).

28. Qian, W. et al. Superhigh electromagnetic interference shielding of ultrathin aligned pristine graphene nanosheets film. *Adv. Mater.* **32**, 1907411 (2020).

29. Savchak, M. et al. Highly conductive and transparent reduced graphene oxide nanoscale films via thermal conversion of polymer-encapsulated graphene oxide sheets. *ACS Appl. Mater. Interfaces* **10**, 3975-3985 (2018).

30. Chen, X. et al. Graphitization of graphene oxide films under pressure. *Carbon N. Y.* **132**, 294-303 (2018).

31. Zhang, G., Shaffer, C. E., Wang, C.-Y. & Rahn, C. D. Effects of non-uniform current distribution on energy density of Li-ion cells. *J. Electrochem. Soc.* **160**, A2299-A2305 (2013).

32. Zhao, Y. et al. Highly reduced graphene assembly film as current collector for lithium ion batteries. *ACS Sustain. Chem. Eng.* **9**, 8635-8641 (2021).

33. Peng, L. et al. Multifunctional macroassembled graphene nanofilms with high crystallinity. *Adv. Mater.* **33**, 2104195 (2021).

34. Wang, B. et al. Ultrastiff, strong, and highly thermally conductive crystalline graphitic films with mixed stacking order. *Adv. Mater.* **31**, 1903039 (2019).

35. Varshney, V., Patnaik, S. S., Roy, A. K., Froudakis, G. & Farmer, B. L. Modeling of thermal transport in pillared-graphene architectures. *ACS Nano* **4**, 1153-1161 (2010).

36. Fu, H. et al. Rapid soldering of flexible graphene assembled films at low temperature in air with ultrasonic assistance. *Carbon N. Y.* **158**, 55-62 (2020).

37. Fu, H. et al. Ultrasonic-assisted soldering for graphite films as heat sinks with durably superior heat dissipating efficiency. *Adv. Compos. Hybrid Mater.* **5**, 2154-2162 (2022).

38. Bernardi, D., Pawlikowski, E. & Newman, J. A general energy balance for battery systems. *J. Electrochem. Soc.* **132**, 5-12 (1985).

39. Du, X. et al. Visualizing two-dimensional internal temperature distribution in cylindrical Li-ion cells. *J. Power Sources* **446**, 227343 (2020).

40. Huang, L. et al. Uncovering LiH triggered thermal runaway mechanism of a high-energy $LiNi_{0.5}Co_{0.2}Mn_{0.3}O_2$/graphite pouch cell. *Adv. Sci.* **8**, 2100676 (2021).

41. Wang, H. et al. Fire and explosion characteristics of vent gas from lithium-ion batteries after thermal runaway: A comparative study. *eTransportation* **13**, 100190 (2022).

42. Scott, G. S., Jones, G. W. & Scott, F. E. Determination of ignition temperatures of combustible liquids and gases. *Anal. Chem.* **20**, 238-241 (1948).

43. Dadbakhsh, S., Mertens, R., Hao, L., Van Humbeeck, J. & Kruth, J. P. Selective laser melting to manufacture "in situ" metal matrix composites: A review. *Adv. Eng. Mater.* **21**, 1801244 (2019).

44. La, P. et al. Bulk nanocrystalline Fe_3Al-based material prepared by aluminothermic reaction. *Adv. Mater.* **18**, 733-737 (2006).

45. Udhayabanu, V., Singh, N. & Murty, B. S. Mechanical activation of aluminothermic reduction of NiO by high energy ball milling. *J. Alloys Compd.* **497**, 142-146 (2010).

46. Hosseini, S. N., Karimzadeh, F. & Enayati, M. H. Mechanochemical synthesis of Al_2O_3/Co nanocomposite by aluminothermic reaction. *Adv. Powder Technol.* **23**, 334-337 (2012).

47. Li, M., *et al.* Graphene: preparation, tailoring, and modification. *Exploration* **3**: 20210233 (2023).

48. Soo, X., Electrospun PEO/PEG fibers as potential flexible phase changematerials for thermal energy regulation. *Exploration* **4**:*2023001* (2024).

49. Dong, L. *et al.* A large-area, flexible, and flame-retardant graphene paper. *Adv. Funct. Mater.* **26**, 1470-1476 (2016).

50. Attia, N. F., Elashery, S. E. A., Zakria, A. M., Eltaweil, A. S. & Oh, H. Recent advances in graphene sheets as new generation of flame retardant materials. *Mater. Sci. Eng. B Solid-State Mater. Adv. Technol.* **274**, 115460 (2021).
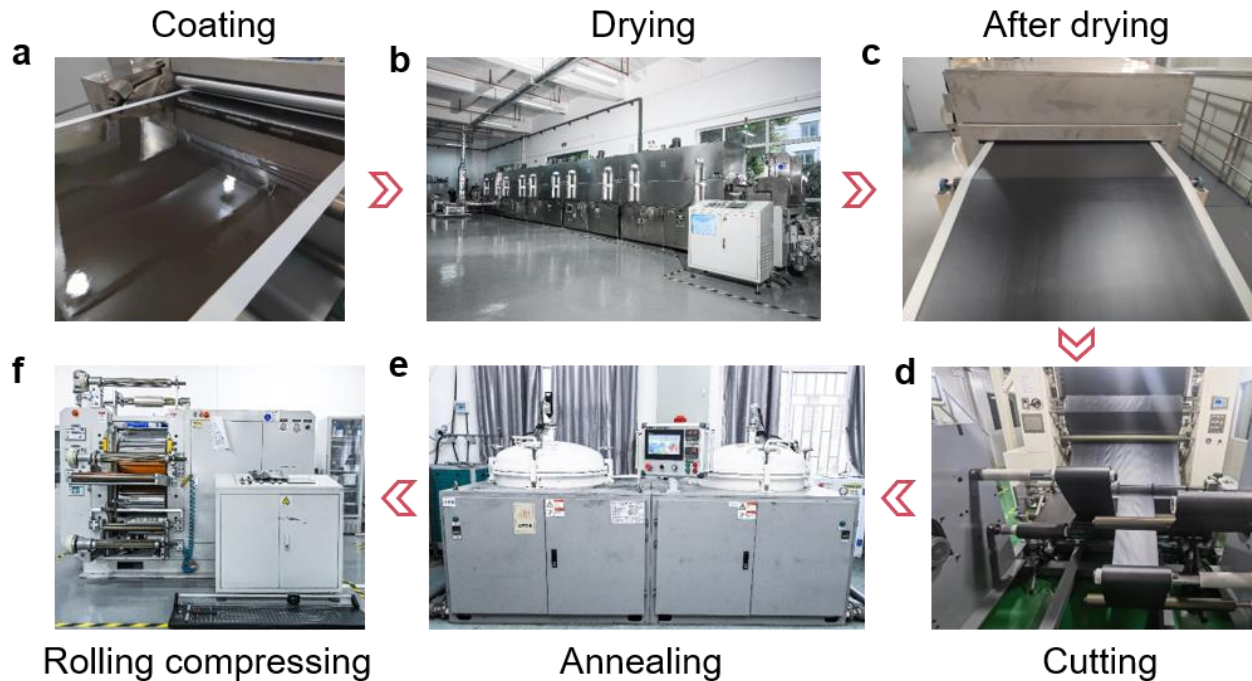
Extended Data Fig. 1 | Fabrication of the large-area Gr foil using GO+3wt.% PEA precursor. a, Coating. **b**, Drying. **c**, Dried precursor film. **d**, Cutting. **e**, Annealing, **f**, Rolling compression.
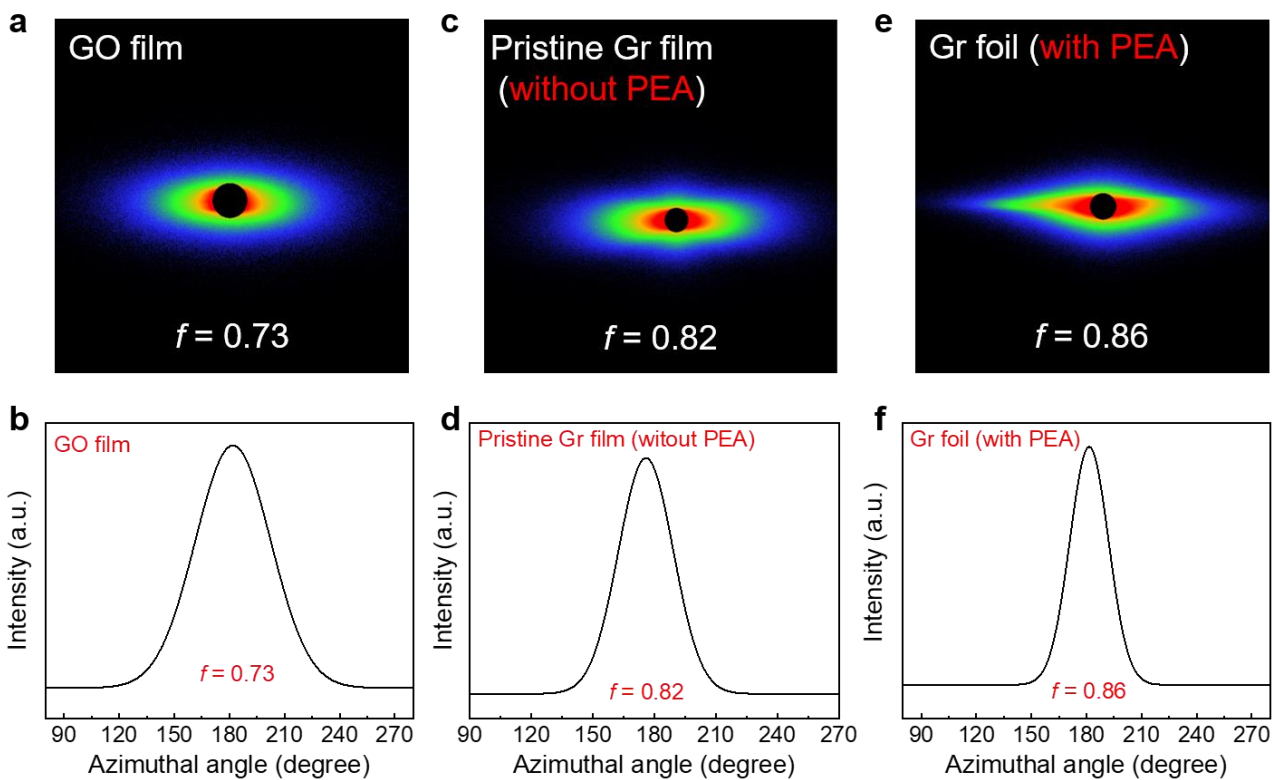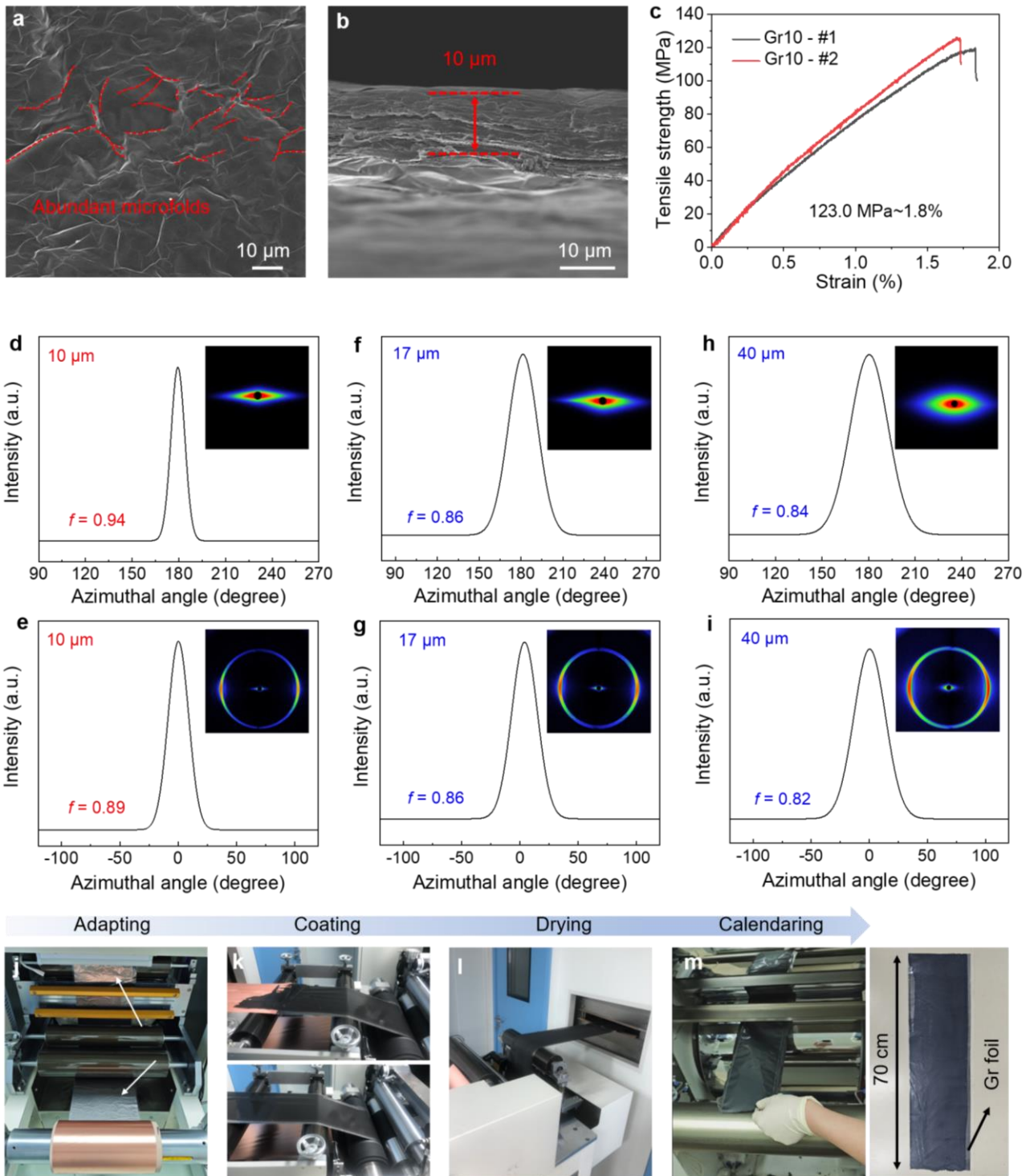
Extended Data Fig. 2 | Characterization of the oriented structure of Gr foils. SAXS patterns and corresponding azimuthal angle plots of **a, b**, GO film. **c**, **d**, pristine Gr film without addition of PEA and **e**, **f** Gr foil with addition of PEA.

5
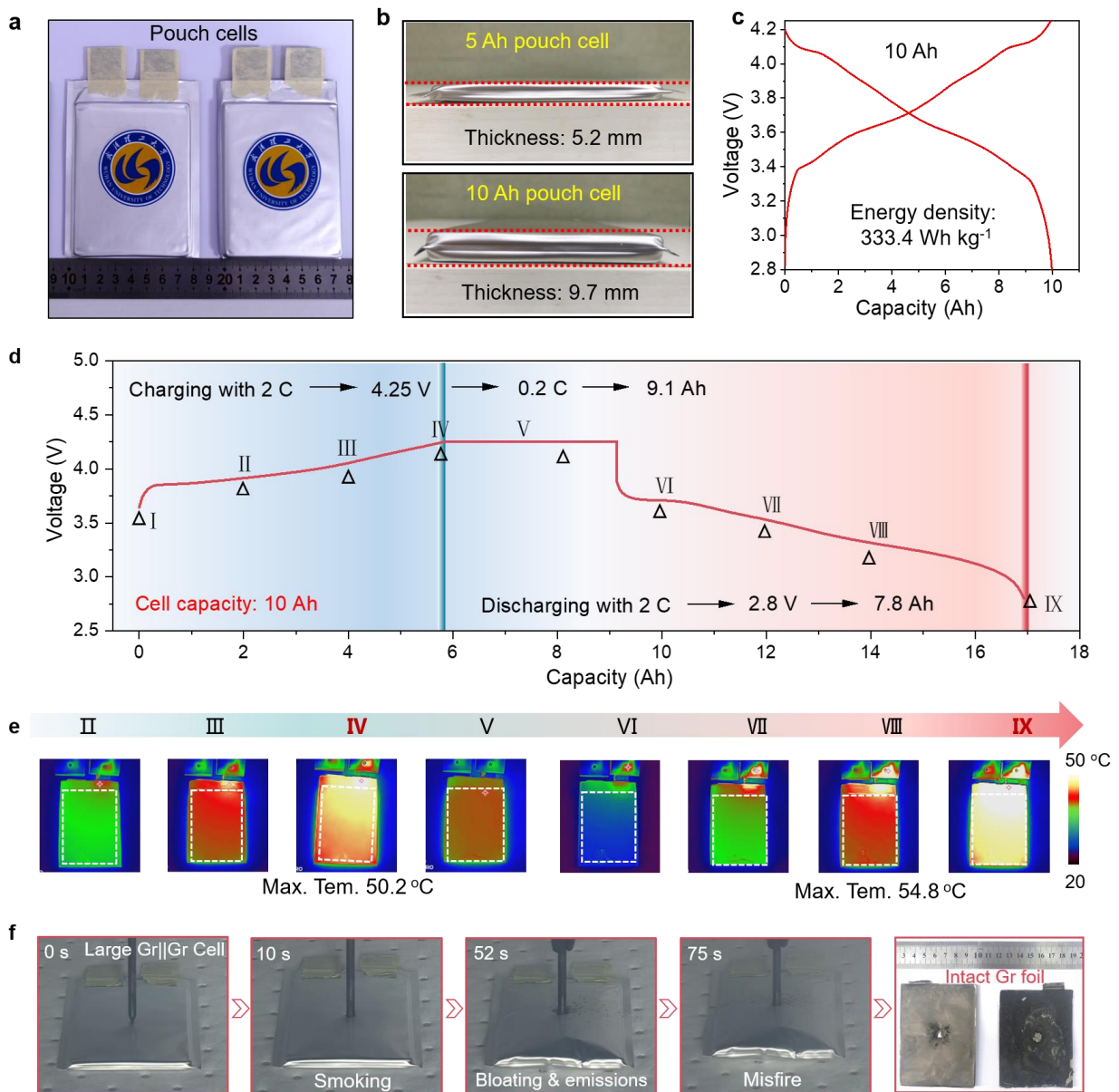
Extended Data Fig. 3 | Electrochemical performance of high-capacity pouch cells. **a**, **b**, Photograph of 5 and 10 Ah pouch cell with Gr CCs. **c**, Charge-discharge curves of 10 Ah pouch cell with Gr||Gr foils at 0.05 C. **d**, Fast charging and discharging profiles at 2 C. **e**, Corresponding temperature distributions at different stages from II to IX. **f**, Nail penetration test on 5 Ah Gr||Gr cell.

5
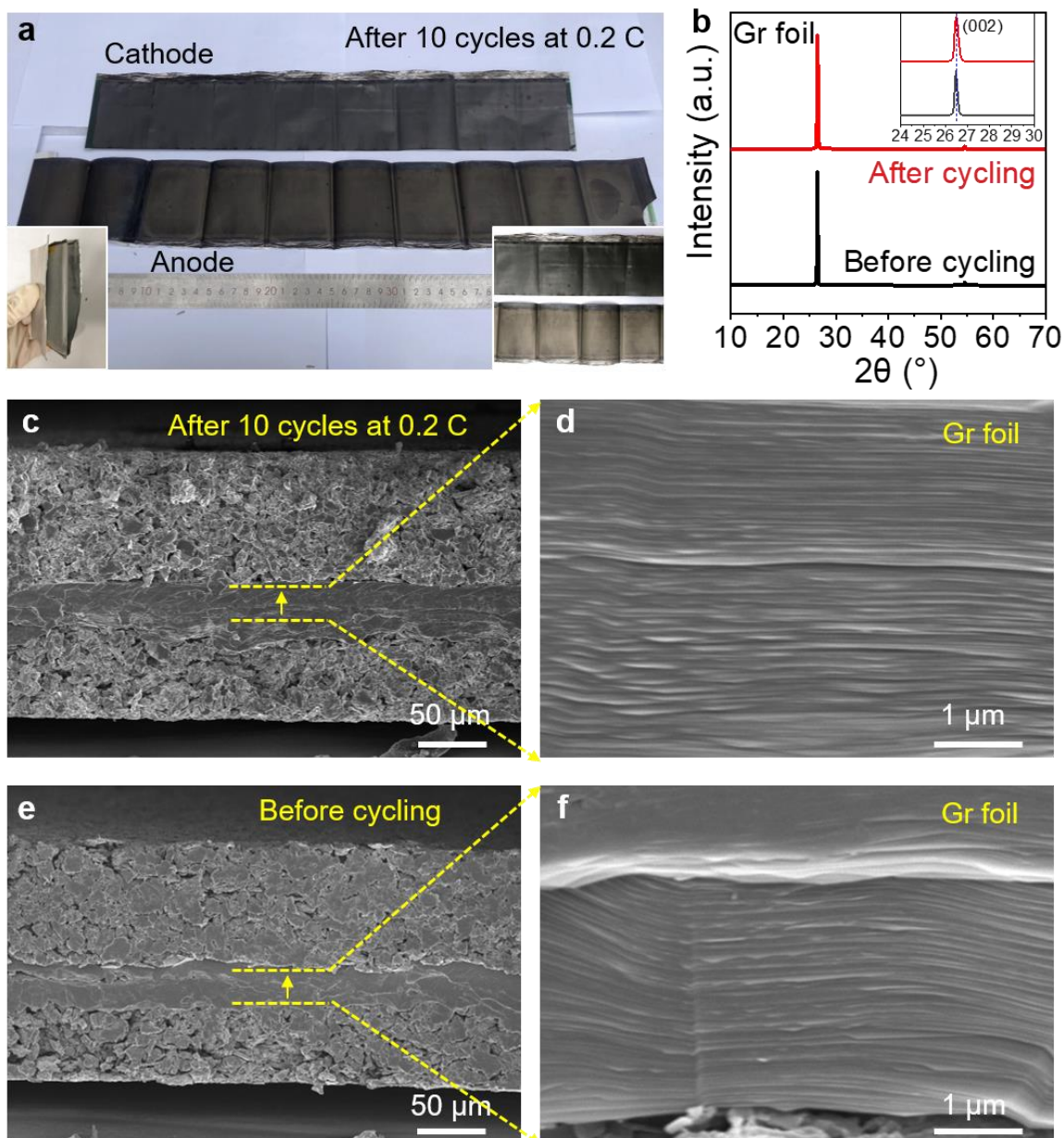
Extended Data Fig. 4 | The electrochemical activity of Gr CCs after cycling in Gr||Gr pouch cells. a, Photograph of the unfolded electrode disassembled from a pouch cell after cycling. **b**, XRD patterns of Gr foil CCs before and after cycling. **c**, Cross-sectional SEM image of the anode layer after cycling at 0.2 C. **d**, Corresponding cross-sectional SEM image of Gr foil CC. **e**, The cross-sectional SEM image of the anode layer before cycling. **f**, The original cross-sectional SEM image of Gr foil before cycling.

Extended Data Fig. 5 | Physical characterization and practical application of 10 μm-thick Gr foil. **a**, Top-view and **b**, cross-sectional SEM images of 10 μm-thick Gr foil. **c**, Stress-strain curves of 10 μm-thick Gr foil. **d**, **f**, **h**, SAXS patterns and corresponding azimuthal angle plots of Gr foils with thickness of (d) 10, (f) 17, and (h) 40 μm. **e**, **g**, **i**, WAXS patterns and corresponding azimuthal angle plots of Gr foils with thickness of (e) 10 μm, (g) 17 μm, and (i) 40 μm. **j-m**, Application of 10 μm-thick Gr foil as CC for (j) adapting in coating machine (Cu foil for traction), (k) electrode coating, (l) electrode drying, and (m) subsequent calendaring process.
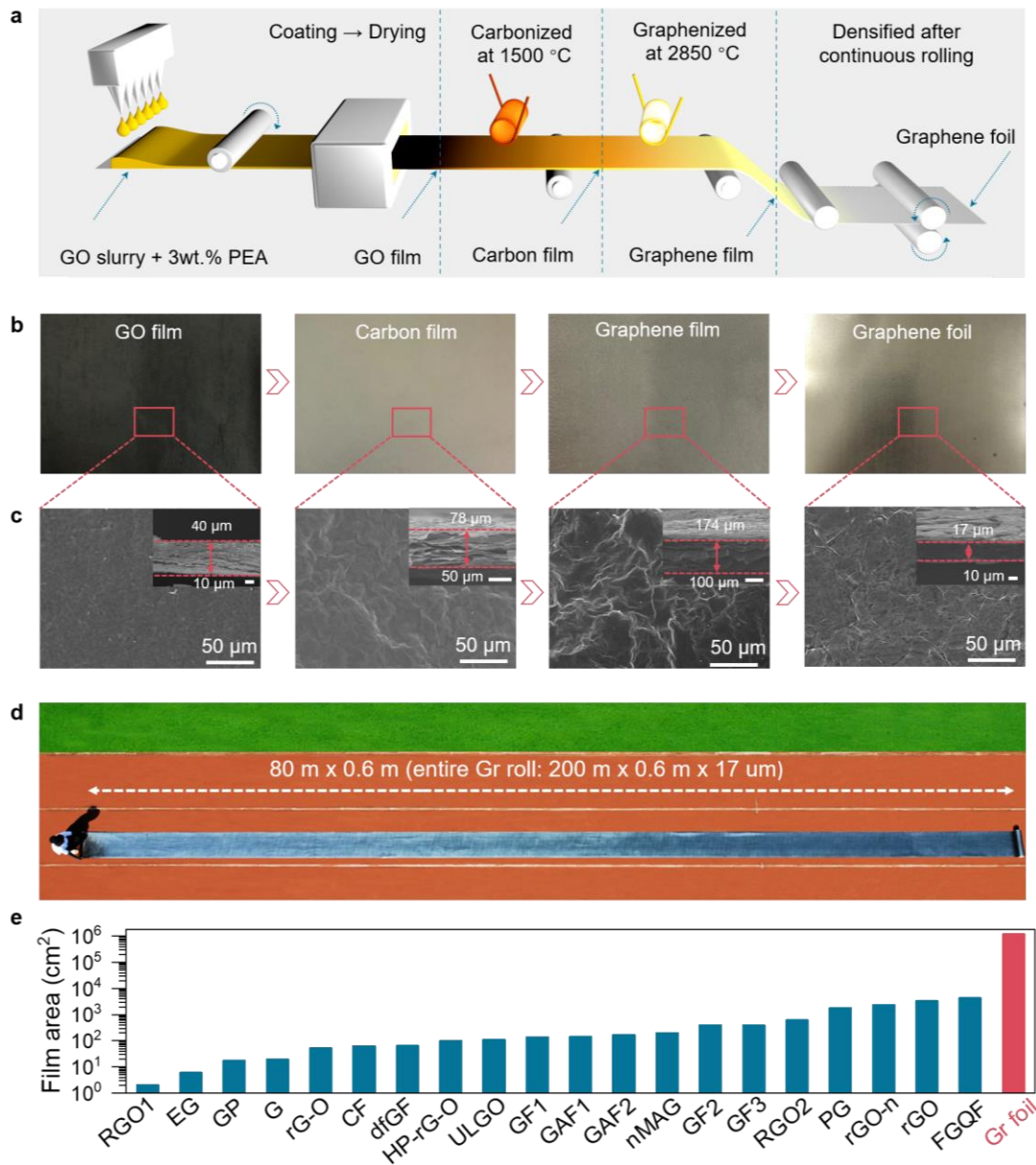
10

Fig. 1 | Fabrication of the large-area Gr foil. a, Schematics showing a continuous thermal pressing process for fabricating Gr foil. **b**, Photos and **c**, surface SEM images of GO film, carbon (C) film, Gr film, and Gr foil, inset: the corresponding cross-sectional images. **d**, Image of large-scale Gr foil (200×0.6 m^2) taken using an unmanned aerial vehicle on the ground of a standard track field. **e**, Comparison of the Gr foil areas produced in this work and to those reported in literatures.
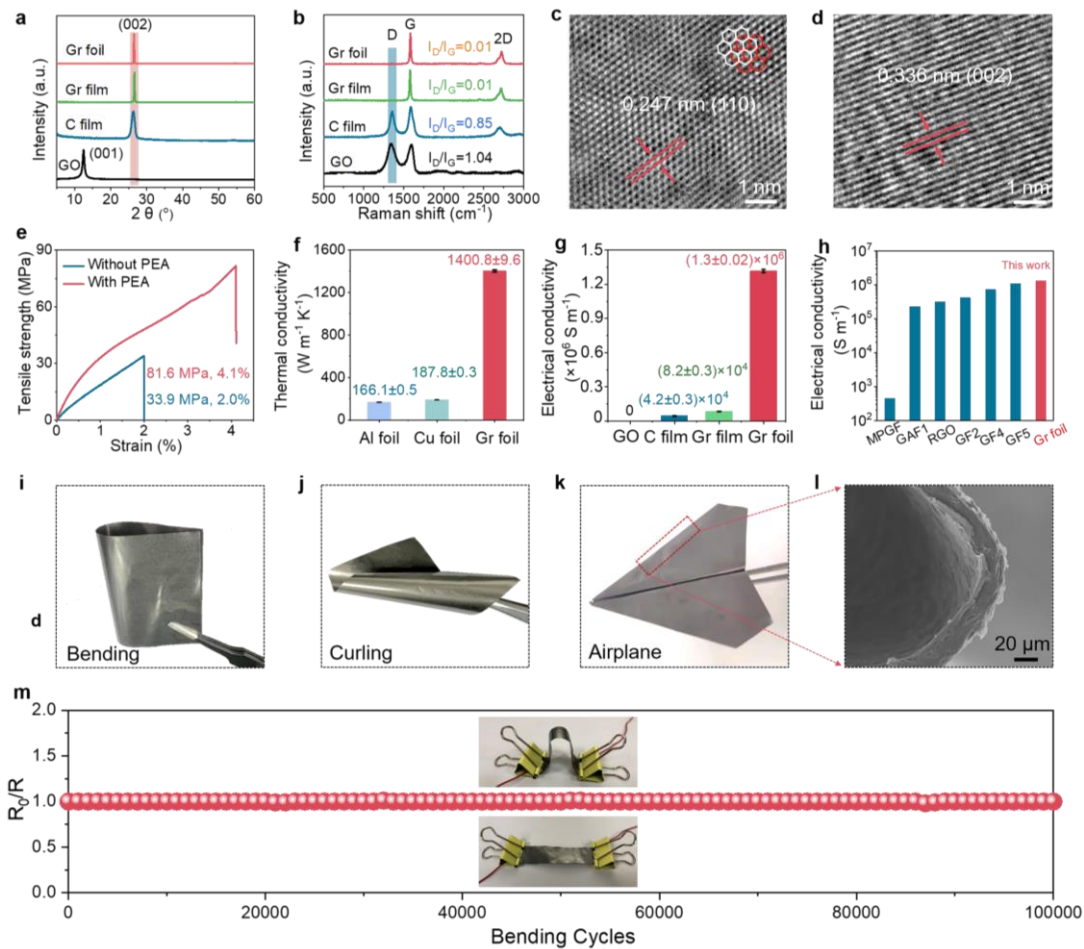
Fig. 2 | Foil physical characterization. a, XRD analysis of GO, C film, Gr film, and Gr foil patterns. **b**, Raman spectra of GO, C film, Gr film, and Gr foil. **c**, High-resolution TEM image of the Gr nanosheets from top-view and **d**, cross-sectional view. **e**, Stress-strain curves of Gr foil. **f**, Thermal conductivities of the Gr foil and the benchmark Al and Cu foils (n=10). **g**, Electrical conductivities of GO film, C film, Gr film and Gr foil (n=10). **h**, Comparison of electrical conductivities of Gr CCs with previously reported values in the literature. Flexibility demonstrations under various deformation conditions: **i**, bending, **j**, curling, **k**, folding into an airplane; **l**, cross-sectional SEM images of Gr foil folded at 180°. **m**, Resistance alternation of Gr with 100,000 repeated bending tests. Data are presented as mean ± SD. The error bars represent standard deviation from ten independent measurements.
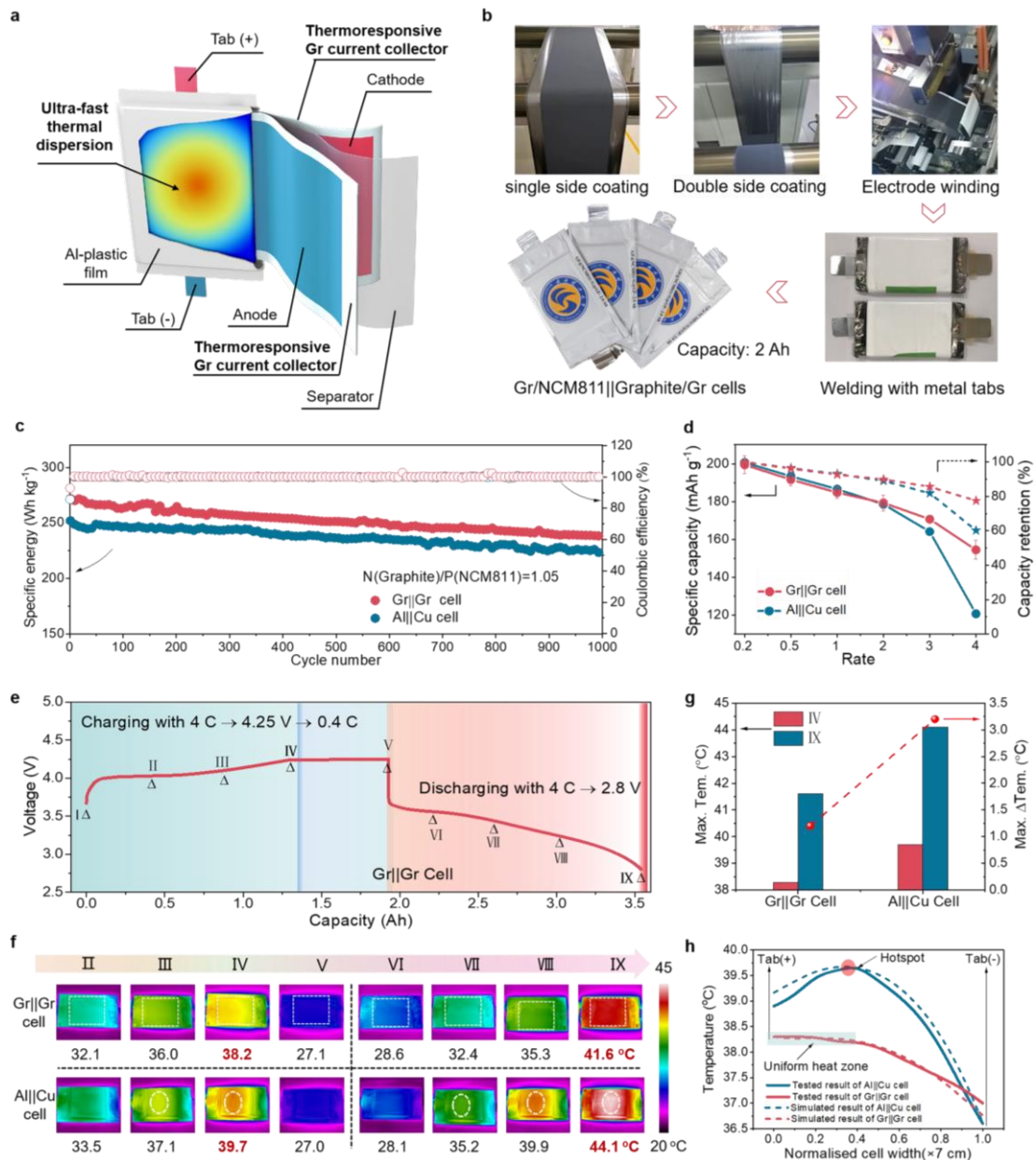
Fig. 3 | Electrochemical and thermal performance. a, Schematic diagram of a pouch cell integrated with Gr CCs. **b**, Assembly of Gr||Gr pouch cells. **c**, Specific energy of pouch cells using Gr||Gr and Al||Cu foils over 1000 cycles at 1 C. **d**, Specific capacity and capacity retention at different current rates from 0.2 to 4 C (n=3). **e**, Fast charging and discharging profiles of a pouch cell with Gr||Gr foils at 4 C. **f**, Temperature distribution at different stages. **g,** Maximum temperatures at stage IV (red bar) and stage IX (blue bar) with the maximum temperature difference (red symbols) at stage IX. **h**, Simulated and experimental thermal behavior for the pouch cells with Gr||Gr and Al||Cu foils at stage IV. Data are presented as mean ± SD. The error bars represent standard deviation from three independent measurements.
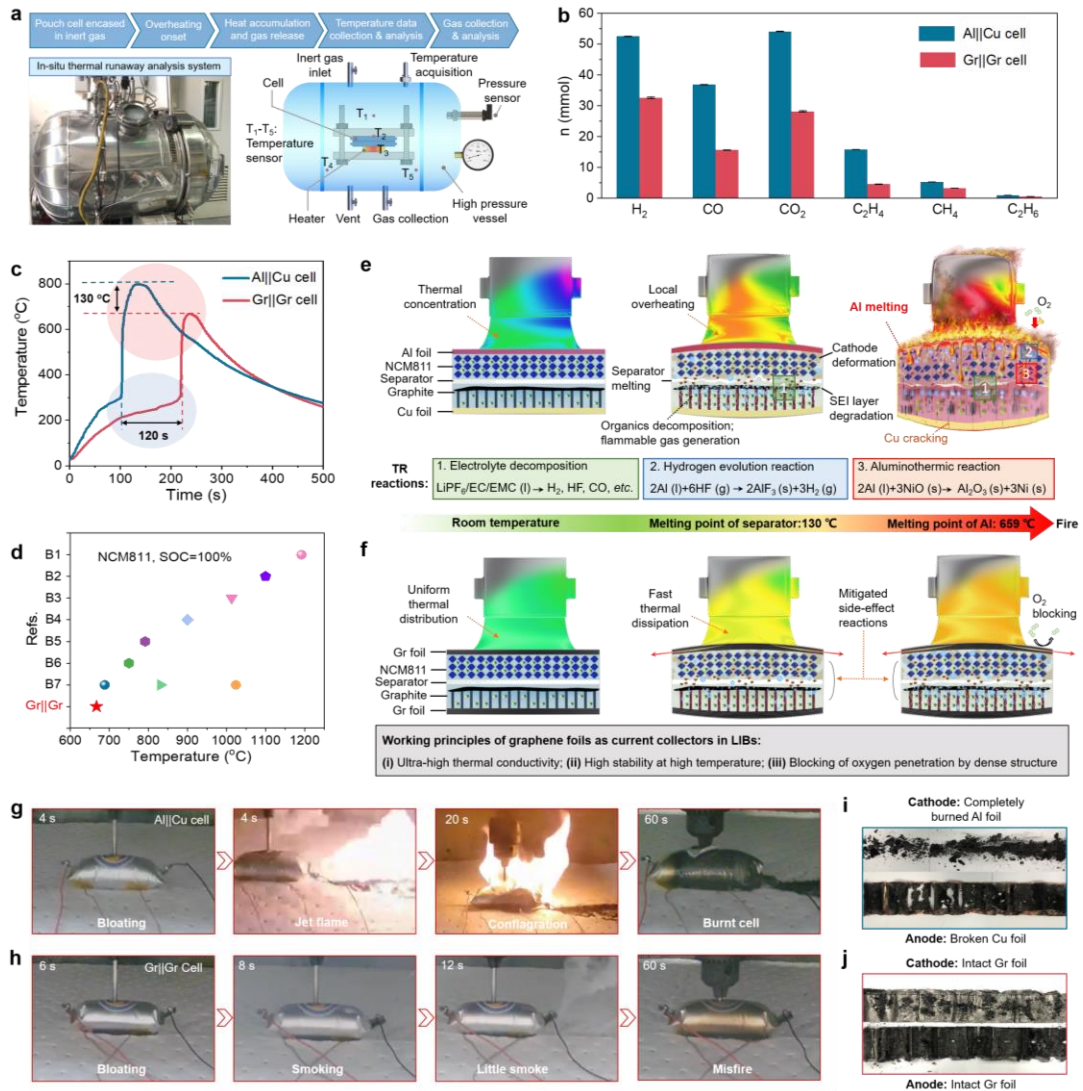
Fig. 4 | Safety performance and mechanism analysis of pouch cells during thermal runaway. a, Schematic diagram of the thermal runaway experimental settings with gas collection and detection. The inset shows the photo of the sealed chamber where thermal runaway occurs. **b**, Specific molar content of each gas composition after thermal runaway for Al||Cu and Gr||Gr pouch cells (n=3). **c**, Temperature profiles of fully charged Al||Cu and Gr||Gr pouch cells during thermal runaway. **d**, Comparison of the battery safety between this work and other publications based on NCM811 cathode under TR. **e**, Incendiary explosion reaction mechanism of Al||Cu cells during thermal runaway. **f**, Safety improvement mechanism of Gr||Gr cells. **g**, **h**, Nail penetration test on the assembled (g) Al||Cu, (h) Gr||Gr pouch cells. **i**, **j**, Unfold electrodes inside (i) Al||Cu and (j) Gr||Gr pouch cells after nail penetration. Data are presented as mean ± SD. The error bars represent standard deviation from three independent measurements.